Superlattices and Microstructures 89 (2016) 398–408

Contents lists available at ScienceDirect

Superlattices and Microstructures

journal homepage: www.elsevier.com/locate/superlattices

Electronic properties of Cantor random box distribution of impurities in graphene

J.S. Ardenghi*, P. Bechthold, P. Jasen, E. Gonzalez, A. Juan

IFISUR, Departamento de Física (UNS-CONICET), Avenida Alem 1253, Bahía Blanca, Argentina

ARTICLE INFO

Article history:
Received 5 September 2015
Received in revised form 24 November 2015
Accepted 25 November 2015
Available online 30 November 2015

Keywords:
Graphene
Cantor set distribution
Random impurities
Electronic density of states

ABSTRACT

The aim of this work is to study the electronic properties of graphene under random impurities which are distributed in the energy line following the Cantor set box distribution. This implies that for each iteration k, the possible energy values of the random impurities lie in the line segment of the Cantor set in the interval $(-\alpha/2,\alpha/2)$. By applying the full T-matrix approximation, the electronic density of states is obtained for each iteration k and the limit $k \to \infty$ limit is taken. A metal-insulator transition is obtained for critical values of α, where a resonance peak in the DOS at the Fermi level is split in two bands that shift towards the band edges when the width α increases. In turn, the electronic density of states for $k \geq 2$ only enhance the van Hove singularities, resonant and anti-resonant states for $k = 2$. In the other side, the Cantor set signatures are shown through a spectrum rearrangement for different values of α, where resonant states split in two narrow peaks for $k = \infty$. These results are important to study the transport properties in graphene with doped-based fractal superlattices, magnetic or electric barriers or multilayers with triadic patterns.

1. Introduction

Graphene is a two dimensional hexagonal lattice of carbon atoms, a newly discovered 2-D allotrope of carbon that has been proved to be much more interesting than any other material known, exhibiting some remarkable properties such as high electric conductivity, high thermal conductivity and extraordinary mechanical strength ([1–5]). The band structure shows that the conduction and valence band touch at the Dirac point and the dispersion relation is approximately linear and isotropic [6]. Due to its linear dispersion relation at low energies, the electrons are turned into effective Dirac fermions [4]. This leads to a number of fascinating phenomena such as the half-quantized Hall effect ([7,8]) and minimum quantum conductivity in the limit of vanishing concentration of charge carriers ([9,1,10]).

Tuning graphene electronic properties to achieve desired functionalities by various adsorbed atoms, molecules and chemically active groups has been a prime research area in modern material science. Through ion bombardment of graphene [11] or deposition of atomic adsorbates ([12,13]) on it, makes it possible to open a quasigap in the nearest vicinity of the Dirac point in the graphene spectrum because the defects induce the impurity resonance states. In turn, graphene samples fabricated are not pristine, therefore is important to understand the effects of disorder on the electronic properties ([14–16]). This disorder manifests itself in the finite lifetime of electronic eigenstates of the pure system. In turn, this may initiate a

* Corresponding author.
E-mail address: jsardenghi@gmail.com (J.S. Ardenghi).

http://dx.doi.org/10.1016/j.spmi.2015.11.033
0749-6036/

metal–insulator transition with massive carriers. These effects can alter the electronic density of states, which is an important property of the system because affects directly many measurable quantities such as the electrical conductivity, thermoelectric effects and differential conductivity in tunneling experiments and modify the electron screening. In the other side, in the last decades, fractal structures has attracted broad attention [17]. Fractals are mathematical sets that that are self-similar across different scales and can be used to describe different physical phenomena or statistical processes. In particular, has attracting much interest in topics related to insulator transitions in condensed matter and systems of cold atoms ([18–20]), Kondo effect in strongly disordered metals [21], renormalization group [22], Lévy flights and quantum critical diffusion [23] and in quantum field theory [24]. Recently, numerous results about electronic transport and modulation properties in fractal structures has been reported, for example the reflection and transmission properties in fractal superlattices [25] or the spectral properties of self-similar optical Fabry-Perot resonator ([26,27]). Non periodic media has been used to study wave propagation ([28,29]). The Cantor set has been applied to quantum scattering in a fractal potential and self-similar structures ([30–34]). In turn, fractal Cantor distributions has been applied to the study of the transmission properties with left-handed materials, showing that these devices can be used as narrow band optical filters with applications in super dense wavelength division multiplexing for optical communications and precise optical measurement [35]. Recently, due to increasing interest in graphene, transport properties in graphene-based fractal structures has been studied, for example in a single layer graphene system under the influence of nanoscale magnetic barriers and wells, which are arranged Cantor pre-fractally or periodically, showing that the angular threshold and angular asymmetry of the transmission spectra are closely related to the ratio between the magnitude of the vector potential and the incident energy [36]. Standard T-matrix method has been used to study the tunneling of Dirac electrons through graphene multilayers, particularly triadic Cantor multilayers, showing that self-similarity and scaling properties appears in the transmittance in graphene deposited on top of slabs of SiO_2 and SiC substrates, where the Cantor series are applied [37].

In this work, we study the electronic properties of Dirac electrons, in particular the electronic density of states, subject to a random distribution of impurities, where the on-site local impurity potentials are given by the Cantor probability distribution. This probability energy distribution of the on-site impurity energies is a generalization of the box distribution of width α. This generalization consists in a distribution which are defined through the sequence of subsets of the Cantor set. That is, for each iteration k of the Cantor set, there will be a probability density distribution for the impurity energies which is not zero in those points defined by the subsets of the k-iteration. This distribution is called the Cantor distribution and whose cumulative distribution function is the Cantor function [38]. In this work, the support of the Cantor set is not the interval [0,1] but the interval $\left[-\frac{\alpha}{2},\frac{\alpha}{2}\right]$, been α an arbitrary energy value. The full-iterated Cantor distribution can be consider as a transition distribution from the n-component random alloy with respective probabilities $c_1, \ldots, c_n$ with $n \to \infty$ and the infinite-component alloy given by the box distribution of width α. In the case that the box distribution is split in several small boxes, the n–component Dirac delta distribution will be obtained in the limit $n \to \infty$. From this viewpoint, the Cantor distribution is a particular choice in which the transition from the box distribution to the infinite-component Dirac delta distribution is obtained. The density of states is computed in terms of the iteration parameter k, using the full T-matrix approximation ([39–41]). For the random Cantor distribution of the on-site impurity energies, how to evaluate the Green's function expansion is not a trivial problem, because the moments of the probability distribution do not yield a tractable closed form and are representable only through computational formulas [29]. In this sense, the main purpose of this work is to track in the density of states the self-similarity of the Cantor set through the iteration parameter k.

This work will be organized as follow: In Section 2, the impurity averaged Green function will be computed for graphene. Although this procedure has been extensively studied and published elsewhere, for a self-contained work it is reproduced. In Section 3 the random Cantor distribution is introduced and the full T-matrix approximation for the self-energy is computed. The electronic density of states are computed for each k and the limit $k \to \infty$ is taken. Within the results, discussions are given and the principal findings of this paper are highlighted in the conclusion.

2. Impurity averaged Green function

The tight-binding clean Hamiltonian of graphene for nearest neighbors reads

$$H_0 = -t\sum_{\mathbf{r}_i}^{N}\sum_{\delta_j}[|\mathbf{r}_i, A\rangle\langle\mathbf{r}_i+\delta_j, B| + |\mathbf{r}_i, B\rangle\langle\mathbf{r}_i+\delta_j, A|] \tag{1}$$

where a sum on the spin σ is understood and t is the nearest neighbor hopping energy. The vectors connecting nearest neighbors are $\delta_1 = \frac{a}{2}(1,\sqrt{3},0)$, $\delta_2 = \frac{a}{2}(1,-\sqrt{3},0)$ and $\delta_3 = a(1,0,0)$, where $a = 0.142\ nm$ is the lattice constant. Impurities can be included in the tight-binding description by the addition of a local energy term

$$H_{imp} = \sum_{\mathbf{r}_i,\sigma}^{N_i}\{V_i|\mathbf{r}_i, A\rangle\langle\mathbf{r}_i, A| + V_i|\mathbf{r}_i+\delta_3, B\rangle\langle\mathbf{r}_i+\delta_3, B|\} \tag{2}$$

where V_i are the on-site impurity potentials and N_i the number of impurities. The local energies V_i are random, characterized by a probability distribution $P(V_i)$. Introducing the Fourier transform $|\mathbf{r}_i\rangle = \frac{1}{\sqrt{N}}\sum_{\mathbf{k},\sigma} e^{i\mathbf{k}\cdot\mathbf{r}_i}|\mathbf{k}\rangle$ [42] and then a change of basis

$\left|\psi_{\lambda=1}\right\rangle = \frac{1}{\sqrt{2}}(|A\rangle - \sqrt{\frac{\phi^*(\mathbf{k})}{\phi(\mathbf{k})}}|B\rangle)$ and $\left|\psi_{\lambda=-1}\right\rangle = \frac{1}{\sqrt{2}}(|A\rangle + \sqrt{\frac{\phi^*(\mathbf{k})}{\phi(\mathbf{k})}}|B\rangle)$, which is a rotation in the sublattice space, where $\phi(\mathbf{k}) = \sum_{\delta_j} e^{i\mathbf{k}\cdot\delta_j}$, Eqs. (1) and (2) reads.[1]

$$H_0 = \sum_{\lambda=\pm1}\sum_{\mathbf{k},\sigma} \lambda\varepsilon(\mathbf{k})|\mathbf{k},\psi_\lambda\rangle\langle\mathbf{k},\psi_\lambda| \tag{3}$$

and

$$H_{imp} = \sum_{\lambda=\pm1}\sum_{\mathbf{k},\mathbf{q},\sigma}^{N} V_{\mathbf{q}}|\mathbf{k}+\mathbf{q},\psi_\lambda\rangle\langle\mathbf{k},\psi_\lambda| \tag{4}$$

where $\varepsilon(\mathbf{k}) = t|\phi(\mathbf{k})|$ and $V_{\mathbf{q}} = \sum_{\mathbf{R}_i,\sigma}^{N_i} \frac{V_i}{N} e^{i\mathbf{q}\mathbf{R}_i}$ is the Fourier transform of the on-site impurity energies V_i. The new basis $|\mathbf{k},\psi_\lambda\rangle$ with $\lambda = +1$ for the conduction band and $\lambda = -1$ for the valence band diagonalize the Hamiltonian H_0 and the eigenvalues are $\varepsilon(\mathbf{k})$ for the conduction band and $-\varepsilon(\mathbf{k})$ for the valence band. In this basis, the clean Green function $G_0 = (z - H_0)^{-1}$ reads

$$G_0^{(\lambda)} = \sum_{\lambda=\pm1}\sum_{\mathbf{k}} \frac{1}{z - \lambda\varepsilon(\mathbf{k})}|\mathbf{k},\psi_\lambda\rangle\langle\mathbf{k},\psi_\lambda| \tag{5}$$

The full Green function is $G^{(\lambda)} = G_0^{(\lambda)}[I - H_{imp}G_0^{(\lambda)}]^{-1}$ and the configurational averaging over the full Green function reads.[2]

$$\begin{aligned} G^{(\lambda)} &= G_0^{(\lambda)} + G_0^{(\lambda)}\langle H_{imp}\rangle_k G_0^{(\lambda)} + G_0^{(\lambda)}\langle H_{imp}G_0H_{imp}\rangle_k G_0^{(\lambda)} + \ldots = G_0^{(\lambda)}\left[I - \Sigma^{(\lambda,k)}G_0^{(\lambda)}\right]^{-1} \\ &= \sum_{\lambda=\pm1}\sum_{\mathbf{k}} \frac{1}{z - \lambda\varepsilon(\mathbf{k}) - \Sigma^{(\lambda,k)}(\mathbf{k})}\left|\mathbf{k},\Psi_\lambda\right\rangle\left\langle\mathbf{k},\Psi_\lambda\right| \end{aligned} \tag{6}$$

where $\Sigma^{(\lambda,k)}$ is the self-energy of Bloch electrons in the conduction-valence basis and the superscript k indicates the number of iterations k in the Cantor random distribution which will be explained in the next section. At this point the configurational averaging over the local energy of the impurities can be taken. Using the T-matrix approximation (see Ref. [39]), the self-energy can be written as[3]

$$\xi^{(\lambda,k)} = \frac{1}{2}\sum_{n=0}^{+\infty}\langle v^{n+1}\rangle_k \eta_\lambda^n(\varepsilon) \tag{7}$$

where $\xi^{(\lambda,k)} = \Sigma^{(\lambda,k)}/E_C$ is the dimensionless self-energy, $v = V/\Delta$ is the dimensionless on-site impurity energy and where

$$\eta^{(\lambda)}(\varepsilon,\gamma) = \int_0^1 \frac{\mathbf{q}d\mathbf{q}}{\varepsilon + i\gamma - \lambda\mathbf{q}} \tag{8}$$

which in the $\gamma \to 0$ limit reads

$$\eta^{(\lambda)}(\varepsilon,\gamma) = -\lambda + \varepsilon\ln\left(\frac{\varepsilon}{\varepsilon-\lambda}\right) - i\frac{\pi}{2}\left(\left|\varepsilon\right| - \varepsilon\frac{|\varepsilon-\lambda|}{\varepsilon-\lambda}\right) \tag{9}$$

where $\varepsilon = E/E_C$ is a dimensionless energy valid up to $|\varepsilon| < 1$ and $\varepsilon(\mathbf{k}) = \hbar v_F\mathbf{k}/E_C$. The energy cutoff is defined as $E_C = \hbar v_F k_C$ where $\pi k_C^2 = (2\pi)^2/A$ where $A = 33a^2/2$ is the area of the hexagonal unit cell (see Ref. [44]) and where $\Delta = \frac{Ak_C^2}{2\pi E_C} = \frac{2}{E_C}$ is a constant with $1/E$ units. The green function of last equation for $\lambda = 1$ gives the linear spectrum for $\varepsilon > 0$ and for $\lambda = -1$ the linear spectrum for $\varepsilon < 0$. The factors $\langle v^{n+1}\rangle_k$ are the $n+1$ moments of the Cantor probability distribution with k-iteration. In the following section this probability will be defined.

3. Random Cantor distribution and full T-matrix approximation

The $n+1$ moments of the probability distribution $P(v)$ are defined as

[1] The same change of basis is introduced in Ref. [43] before Eq. (6).
[2] The new basis $|\psi_{\lambda=-1}\rangle$ and $|\psi_{\lambda=1}\rangle$ do not depends on V_i, then the configurational averaging can be taken over the matrix elements.
[3] In this approximation we are not taking into account nested diagrams.

$$\langle v^n\rangle_k = \int v^n P_k(v)dv \tag{10}$$

In general, for binary, Gaussian or rectangular distribution, Eq. (7) can be analytically solved, where $\langle v^n\rangle_k$ has a simple functional form in term of the moment of the distribution. In this work we want to explore a modification of the rectangular distribution which consist in an probability distribution given by the Cantor set in the energy line. That is, the probability distribution is not zero-valued in those points which are the Cantor set that can be defined in the [0,1] interval of the real line (see Ref. [45]), which is the Cantor distribution whose cumulative distribution function is the Cantor function [38]. The subset of each iteration k can be written as

$$C_k = \bigcup_{j=0}^{3}\bigcup_{i_1=0}^{1}\cdots\bigcup_{i_{k-1}=0}^{1}\left\{\frac{j+2\beta_k}{3^k}\right\} \tag{11}$$

where k is the $k^{th}-$ step of the iteration and $\beta_k = \sum_{s=1}^{k-1} 3^s i_s$.[4] Using the last equation, the possible energy values of the impurities are random variables with a probability distribution of width α in the interval $(-\alpha/2,\alpha/2)$ (see Fig. 1).[5]

Then, the moments $\langle v^n\rangle_k$ are defined as follows

$$\langle v^n\rangle_k = \frac{1}{N_k}\sum_{i_1=0}^{1}\cdots\sum_{i_{k-1}=0}^{1}\sum_{l=0}^{1}\int_{\alpha\left[\frac{2l(1-\delta_{k,0})+1+2\beta_k(1-\delta_{k,0})(1-\delta_{k,1})}{3^k}-\frac{1}{2}\right]}^{\alpha\left[\frac{2l(1-\delta_{k,0})+2\beta_k(1-\delta_{k,0})(1-\delta_{k,1})}{3^k}-\frac{1}{2}\right]} v^n dv \tag{12}$$

where N_k is the normalization factor and reads

$$N_k = \sum_{i_1=0}^{1}\cdots\sum_{i_{k-1}=0}^{1}\sum_{l=0}^{1}\int_{\alpha\left[\frac{2l(1-\delta_{k,0})+1+2\beta_k(1-\delta_{k,0})(1-\delta_{k,1})}{3^k}-\frac{1}{2}\right]}^{\alpha\left[\frac{2l(1-\delta_{k,0})+2\beta_k(1-\delta_{k,0})(1-\delta_{k,1})}{3^k}-\frac{1}{2}\right]} dv = \alpha\left(\frac{2}{3}\right)^k \tag{13}$$

which is the total length of the Cantor set $\left(\frac{2}{3}\right)^k$ multiplied by the energy width α as it is expected. Eq. (12) can be written in a more useful form as follows

$$\langle v^n\rangle_k = \frac{1}{N_k}\frac{\alpha^{n+1}}{n+1}\chi_n^{(k)} \tag{14}$$

where the coefficients $\chi_n^{(k)}$ reads

$$\chi_n^{(k)} = \sum_{i_1=0}^{1}\cdots\sum_{i_{k-1}=0}^{1}\sum_{l=0}^{1}\left[\left(\frac{2l(1-\delta_{k,0})+1+2\beta_k(1-\delta_{k,0})(1-\delta_{k,1})}{3^k}-\frac{1}{2}\right)^{n+1} - \left(\frac{2l(1-\delta_{k,0})+2\beta_k(1-\delta_{k,0})(1-\delta_{k,1})}{3^k}-\frac{1}{2}\right)^{n+1}\right] \tag{15}$$

In this work we have computed up to $\chi_{12}^{(k)}$. The odd terms are zero due to the symmetry of the probability distribution. In Appendix A we show how to obtain $\chi_2^{(k)}$ and the procedure for the remaining factors $\chi_j^{(k)}$ is straightforward. The values found for $\chi_2^{(k)}$ reads

$$\chi_2^{(0)} = \frac{1}{4}\quad \chi_2^{(1)} = \frac{13}{54}\quad \chi_2^{(k>1)} = 2^{k-2}3^{-3k}\left(2\cdot 3^{2+k} + 16\cdot 3^{2k+1} - 41\right) \tag{16}$$

In Fig. 2, $\chi_2^{(k)}$ and $\chi_4^{(k)}$ are plotted as a function of the iteration parameter k. A maximum is obtained for $k=2$, although when the function $\chi_2^{(k)}$ is multiplied by $(3/2)^k$, $\langle v^2\rangle_k$ tends to a finite value for $k\to\infty$, $\langle v^2\rangle_\infty = 4\alpha^2$. In typical cases such as binary random alloy or box distribution, Eq. (7) can be solved analytically and the result is suitable to obtain the self-consistent equation for the self-energy which takes into account nested diagrams [46]. In the case of the Cantor random

[4] For k=0 and k=1, and β_1=0.

[5] As v is a dimensionless constant, then so is α.

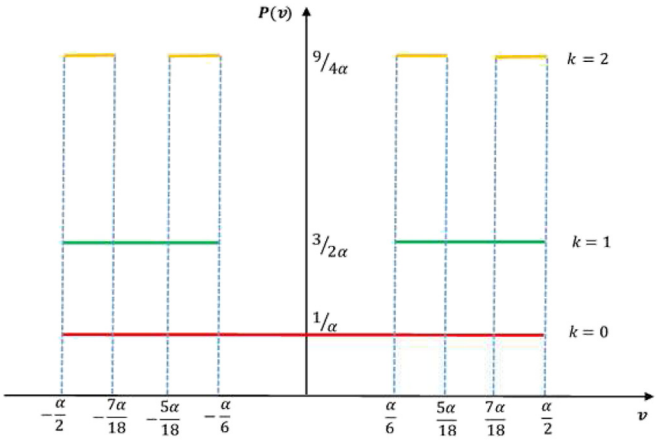

Fig. 1. The Cantor set box distribution for the first three iterations.

distribution, it is not possible to obtain a closed formula for Eq. (7), then the validity of the approximation in this section is guaranteed for $\alpha < 1$. Finally, using Eq. (6), the dimensionless density of states $\rho^{(k)} = -\frac{1}{\pi}\sum_{\lambda=\pm1}\Im Tr(G_\lambda)$ (see Refs. [47,48]) reads

$$\begin{aligned}\rho^{(k)} = -\frac{1}{\pi}\sum_{\lambda=\pm1}\Bigg[&2\left(\xi_R^{(\lambda,k)}-\varepsilon\right)\left(\arctan\left(\frac{\xi_R^{(\lambda,k)}-\varepsilon}{\xi_I^{(\lambda,k)}}\right)-\arctan\left(\frac{\left(\xi_R^{(\lambda,k)}-\varepsilon+\lambda\right)}{\xi_I^{(\lambda,k)}}\right)\right)\\&+\xi_I^{(\lambda,k)}\ln\left(\frac{\left(\xi_I^{(\lambda,k)}\right)^2+\left(\xi_R^{(\lambda,k)}-\varepsilon+\lambda\right)^2}{\left(\xi_I^{(\lambda,k)}\right)^2+\left(\xi_R^{(\lambda,k)}-\varepsilon\right)^2}\right)\Bigg]\Bigg[2\left(\xi_R^{(\lambda,k)}\right)\left(\arctan\left(\frac{\xi_R^{(\lambda,k)}}{\xi_I^{(\lambda,k)}}\right)-\arctan\left(\frac{\left(\xi_R^{(\lambda,k)}+\lambda\right)}{\xi_I^{(\lambda,k)}}\right)\right)\\&+\xi_I^{(\lambda,k)}\ln\left(\frac{\left(\xi_I^{(\lambda,k)}\right)^2+\left(\xi_R^{(\lambda,k)}+\lambda\right)^2}{\left(\xi_I^{(\lambda,k)}\right)^2+\left(\xi_R^{(\lambda,k)}\right)^2}\right)\Bigg]\end{aligned} \tag{17}$$

In Fig. 3, the DOS for different values of α and for $k = 0$, $k = 1$ and $k = 2$ values is shown as a function of ε. For $\alpha = 0.1$ to $\alpha = 0.3$ and for the $k = 0$ and $k = 1$, the DOS retain the linear dispersion relation, but for $k = 2$ there is a spectrum rearrangement between $\alpha = 0.1$ and $\alpha = 0.4$. The behavior obtained for $k > 2$, for different values of the width α, only enhance the electronic properties that appear for $k = 2$, then these results are not shown in Fig. 3. For $\alpha = 0.3$, a large peak at $\varepsilon = 0$ is found and two symmetric peaks for $\varepsilon = \pm 0.3$ are obtained. At this point, doped graphene shows a metallic phase. In turn, for $k = 0$ and $k = 1$ there is no band splitting, unlike the DOS curve for $k = 2$, which shows a splitting for $\alpha > 0.4$. The behavior for $k = 0$ and $k = 1$ is the behavior expected for a box distribution and where the unique effect of neglecting the middle part of the

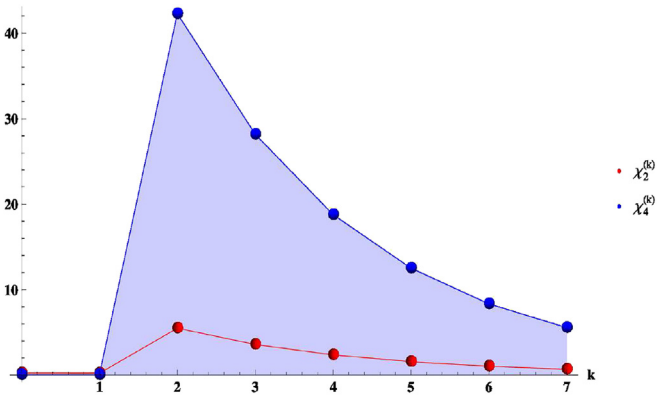

Fig. 2. Curves $\chi_2^{(k)}$ and $\chi_4^{(k)}$ as a function of the iteration parameter k.

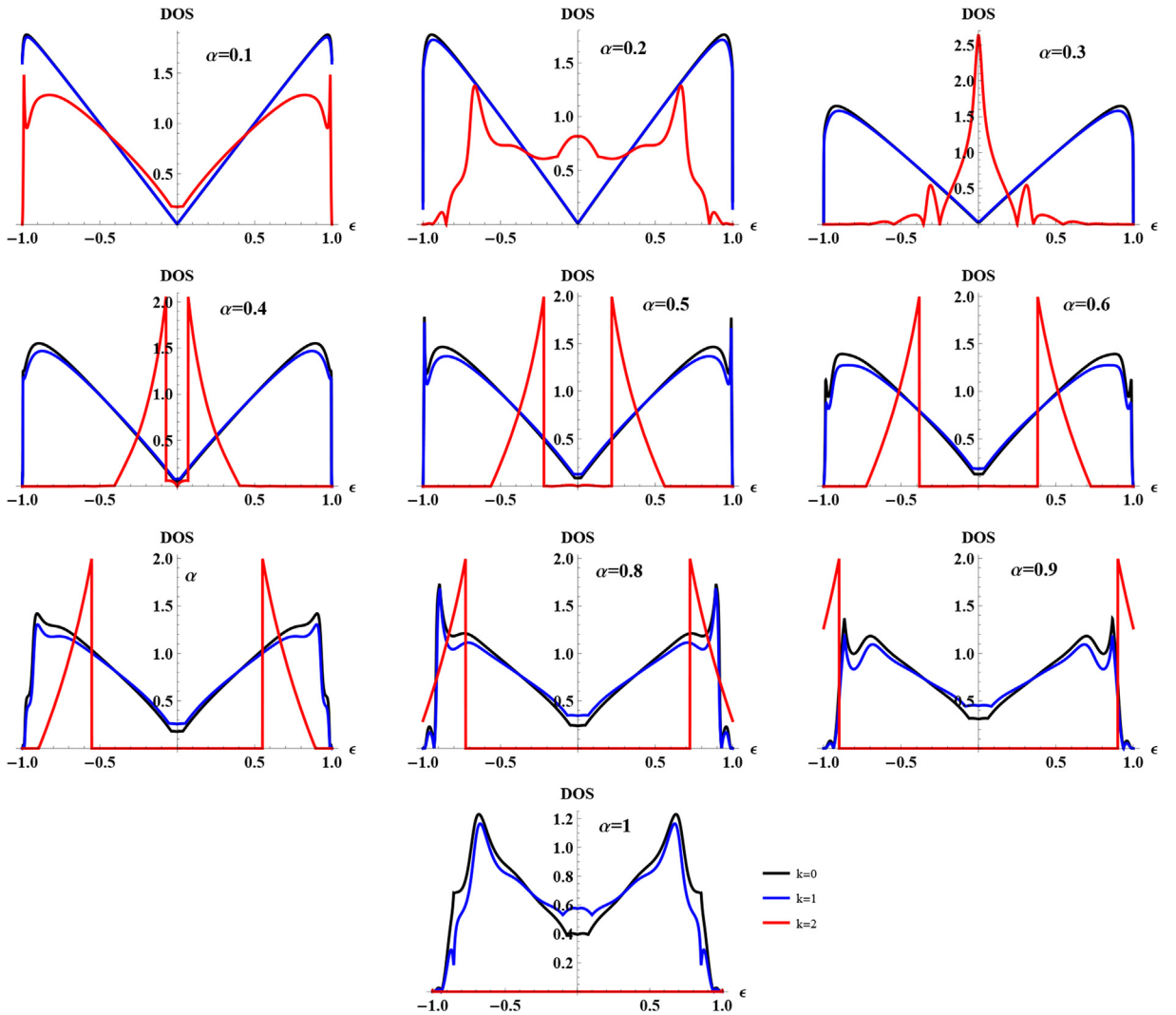

Fig. 3. Density of states for different values of α and $k = 0$ (black), $k = 1$ (blue) and $k = 2$ (red). (For interpretation of the references to color in this figure legend, the reader is referred to the web version of this article.)

uniform distribution is to enhance the DOS at the Fermi level and to reduce it at the band edges. In the other side, for $k \geq 2$ the DOS presents two van Hove singularities that are shifted towards the band edges for larger α. The resonant peak at the Fermi level for $\alpha = 0.3$ and $k = 2$ is similar to those found in Ref. [49] which reflects the formation of new states located at the Fermi level, which is understood as the formation of a new band. In Fig. 4, the DOS is shown only for $k = 2$ and larger values of α. As it can be seen, there are two symmetric set of resonant peaks that decrease when α increases and three symmetric points where the DOS vanishes, which implies a transition of a semi-metallic to metallic behavior when the Fermi level crosses the maximum and minimum of the DOS curve. The qualitative change obtained between $k \leq 1$ and $k \geq 2$ can be traced in the ratio $\frac{\chi_n^{(k)}}{\left(\frac{2}{3}\right)^k} / \frac{\chi_n^{(k+1)}}{\left(\frac{2}{3}\right)^{k+1}} \ll 1$ for $k \geq 1$, which implies a larger contribution to the self-energy from the coefficients $\chi_n^{(k)}/N_k$. The resonant peak at the Fermi level can be understood by noting that $\rho^{(k)} = -\frac{1}{\pi} \sum_{\lambda=\pm 1} \eta_I(\varepsilon - \xi_R^{(\lambda,k)}, \xi_I^{(\lambda,k)})$, then for ε~0, $\xi_I^{(\lambda,k)} = 0$ and the DOS can be written

$$\rho^{(k)}(0) = -\frac{1}{\pi} \sum_{\lambda=\pm 1} \int_0^1 \delta\Big(- \lambda \mathbf{q} - \xi_R^{(\lambda,k)}(0)\Big) \mathbf{q} \mathbf{d}\mathbf{q} = \langle v^2 \rangle_k \left[1 - \frac{\left| \langle v^2 \rangle_k - 1 \right|}{\langle v^2 \rangle_k - 1} \right] \tag{18}$$

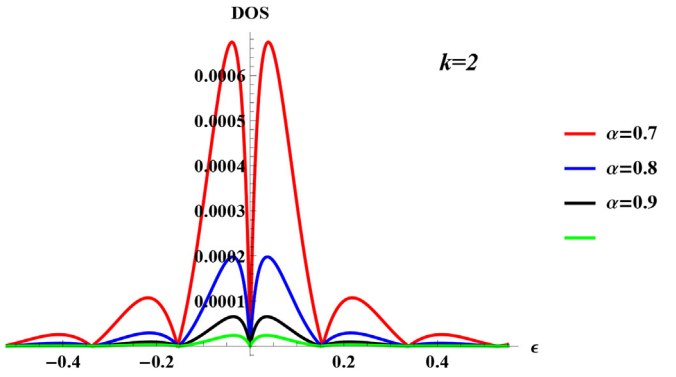

Fig. 4. Density of states for $\alpha = 0.7$ (red), $\alpha = 0.8$ (blue), $\alpha = 0.9$ (black) and $\alpha = 1$(green) for $k = 2$ in the interval near the Fermi level. (For interpretation of the references to color in this figure legend, the reader is referred to the web version of this article.)

where we have used that $\xi_R^{\lambda}(0) = -\lambda\langle v^2\rangle_k$ at low order in α. The density of states at the Fermi level is zero when $\langle v^2\rangle_k > 1$ and $\rho^{(k)}(0) \sim 2\langle v^2\rangle_k$ when $\langle v^2\rangle_k < 1$, then the critical point at which the system behaves as a metal is given by $\langle v^2\rangle_k = 1$, since the electrical conductivity is directly proportional to the density of states at the Fermi level [50]. For $k = 0$ and $k = 1$, this equation has no solution for $|\alpha| < 1$ and for $k = 2$, $\alpha_C = \sqrt{\frac{972}{4009}} \sim 0.492$. From Fig. 3, the metallic phase is obtained for α~0.3 which is below the critical value α_C, which implies that the next order in $\xi^{(\lambda,k)}$ must be taken into account. The energy values where the wavefunction is localized are found by using the dispersion relation $\lambda\mathbf{q} = \varepsilon - \xi^{(\lambda,k)}(\varepsilon)$ which enables to obtain the mean free path l as the inverse of the imaginary part of the wave vector (see Ref. [51], page 155)

$$l^{(k)} = \frac{1}{2|\mathbf{q}_I^{(k)}|} \sim \frac{1}{\pi\varepsilon\langle v^2\rangle_k} \tag{19}$$

which means that states at the band center are extended. For $k = 0$, $l^{(0)} = \frac{12}{\pi\varepsilon\alpha^2}$, for $k = 1$, $l^{(0)} = \frac{108}{13\pi\varepsilon\alpha^2}$ and for general $\lim_{k\to\infty} l^{(k)} = \frac{1}{4\pi\varepsilon\alpha^2}$ which implies that the Cantor distribution decreases the mean free path $l^{(\infty)} \sim \frac{1}{48} l^{(0)}$.

To obtain an approximate behavior of the electronic properties of graphene in the full-iterated Cantor distribution, we can proceed as follows: the coefficients $\chi_n^{(k)}/N_k$ have a finite limit for $k \to \infty$, which correspond to the case in which the total energy length from $-\alpha/2$ to $\alpha/2$ has been removed, although it is well known that an infinite number of energy values remains which are available for the random impurities. Because we have computed $\chi_n^{(k)}$ up to $n = 12$, the limits obtained are

$$\Phi(n) = \lim_{k\to\infty} \frac{\alpha\chi_{2n}^{(k)}}{N_k} = \left\{12, \frac{3037}{32}, \frac{2220241}{3328}, \frac{24805792449}{5457920}, \frac{178732981355897}{5859622912}, \frac{24264081186973132831}{119770692321280}, \ldots\right\} \tag{20}$$

Because it is not possible to obtain an explicit formula for $\chi_n^{(k)}$, neither for the sequence of numbers of the limit $\frac{\alpha\chi_n^{(k)}}{N_k}$ for $k \to \infty$, then a different approach must be taken. It is possible to obtain the best-fitting curve for the set of points obtained in last equation, in particular the following function has been chosen

$$\Phi(n) = \lim_{k\to\infty} \frac{\alpha\chi_n^{(k)}}{N_k} \sim \left(a + bn + cn^2\right)e^{dn} + f + hn + pn^2 + tn^3 \tag{21}$$

where $f = 1.01011$, $h = 1.02286$, $p = 1.04611$, $t = 1.06653$, $d = 1.61276$, $a = 1.0444$, $b = 0.68461$ and $c = 0.203203$.

Using the fitting function of the last equation, the self-energy can be computed using Eq. (7) as follows (see Fig. 5)

$$\begin{aligned}\xi^{(\lambda,\infty)} &= \alpha\sum_{n=1}^{+\infty}\frac{\left(\alpha\eta^{(\lambda)}\right)^{2n-1}}{2n+1}\Phi(n)\\ &= \frac{1}{24\alpha\eta^2}\left[8\alpha^3\eta^3 t_4 F_3\left(\frac{3}{2},2,2,2;1,1,\frac{5}{2};\alpha^2\eta^2\right) + 6e^{-d/2}(4a-2b+c)\tanh^{-1}\left(\alpha\eta e^{d/2}\right) + 6\tanh^{-1}(\alpha\eta)(4f-2h+p)\right.\\ &\quad \left. + 6\alpha\eta\left(-4a - \frac{\alpha^2\eta^2 e^d(2b-3c)-2b+c}{\left(\alpha^2\eta^2 e^d-1\right)^2} - 4f + \frac{\alpha^2\eta^2(3p-2h)+2h-p}{\left(\alpha^2\eta^2-1\right)^2}\right)\right]\end{aligned} \tag{22}$$

where ${}_pF_q(a_1,\ldots,a_p;b_1,\ldots b_q;z)$ is the generalized hypergeometric function of p parameters of type 1 and q parameters of type 2. Finally, using Eq. (17) and Eq. (22), the density of states for different values of α can be obtained as it is shown in Figs. 6–8.

In the limit $k \to \infty$, the electronic density of states at the Fermi level increases between $\alpha = 0$ and $\alpha = 3$ (see Fig. 6) and a band splitting occurs for $\alpha > 0.3$ as it can be seen in Figs. 7 and 8. It can be seen that a van Hove singularity in the conduction and valence band for $\alpha > 0.3$ appears and its position gradually shifts away the band edge. In general, in normal 2D systems

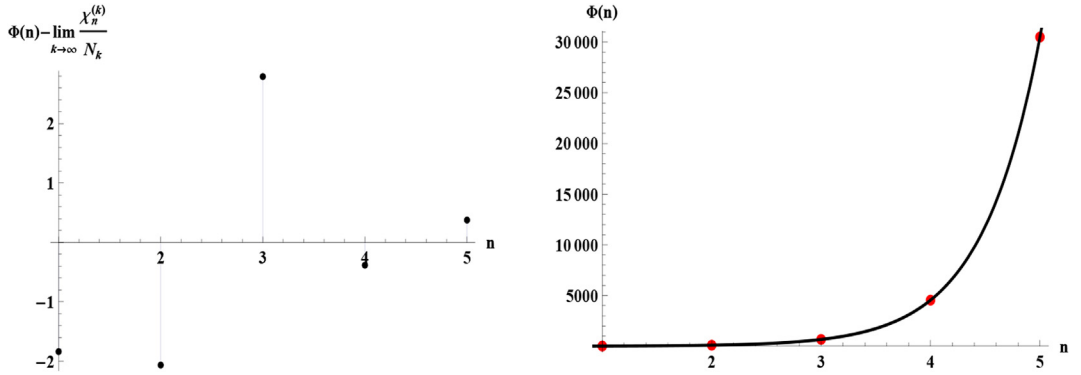

Fig. 5. Left. Residuals of the fitting curve for the first points used to obtain the best approximation to $\Phi(n)$. Right. Fitting curve and points of $\Phi(n)$.

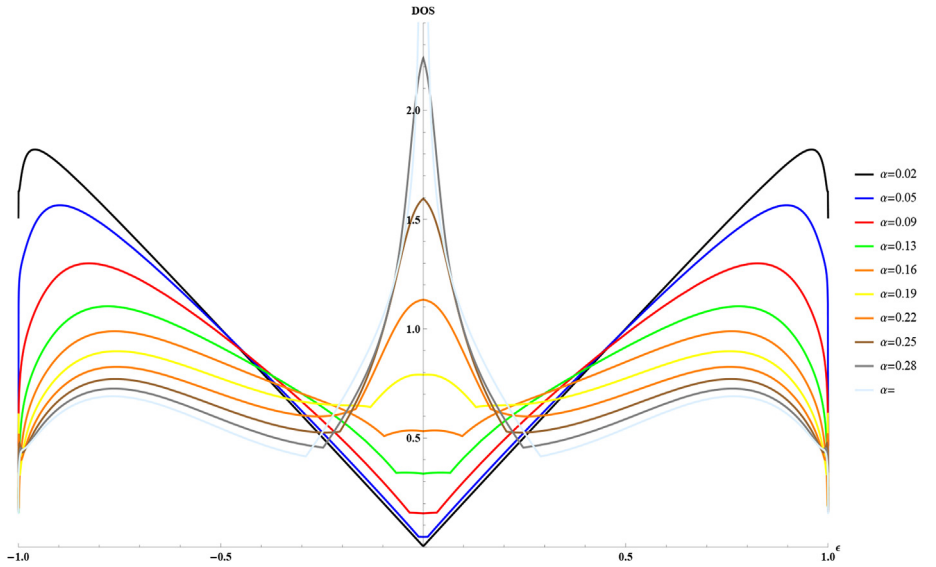

Fig. 6. Density of states for different values of α between 0 and 0.31 and for $k \to \infty$.

with disorder, a band tail appears above the band edge in the valence band and the conduction band. Then the density of states in the presence of defects is reduced for lower energies than the Fermi energy because more states are available in the band tail. In graphene, the valence and conduction band touches at the Dirac point, then the band tail cannot be formed, which produces an enhancement of the density of states below and above the Fermi level when the parameter α increases. In Fig. 7, the system approach a Mott transition. This transition from a metal to a band insulator is the precursor of a divergence in the DOS at the Fermi level. The main difference is that after the driven Mott transition, the Cantor distribution signature appears below and above the Fermi level as it can be seen in Fig. 8. For larger α, new resonances appear symmetrically to the Fermi level that split again in two quasi-localized states. The fact is that the electronic density of states must reproduce in some sense the purely singular spectrum of the impurities that has infinitely many holes. The modifications that the Cantor impurity distribution introduces in the elementary excitation spectrum can lead to a spectrum rearrangement in the vicinity of the Fermi level position due to the presence of the successive non-overlapping dispersion branches of the Cantor subset in the spectrum, which can be separated by a mobility gap. This overlap results in a radical alteration of the spectral properties of graphene in a Cantor distribution after reaching the Mott transition, which is especially pronounced near the Fermi level [52].

Before concluding we point out that our perturbative calculation of the electronic density of states assumes that the system remains homogeneous in the presence of impurities. But it was shown that graphene carriers develop strong density inhomogeneous at low enough carrier densities in the presence of impurities due to the breakdown of linear scattering ([53,54]). A rough approximation of the effects can be done if we consider the concentration of impurities $c = N_i/NA$, the effective decay radius of an impurity state is $r_{imp} \sim \langle v^2 \rangle_k$ ([55,56]).[6] In turn, the average distance between impurities depends

[6] In those papers, $r_{imp} \sim \langle v \rangle_k$, but for the Cantor distribution, the first contribution is $\langle v^2 \rangle_k$. If we consider the coherent potential approximation, the effective medium will contain only one impurity and $\langle v^2 \rangle_k$ will play the role of the effective potential.

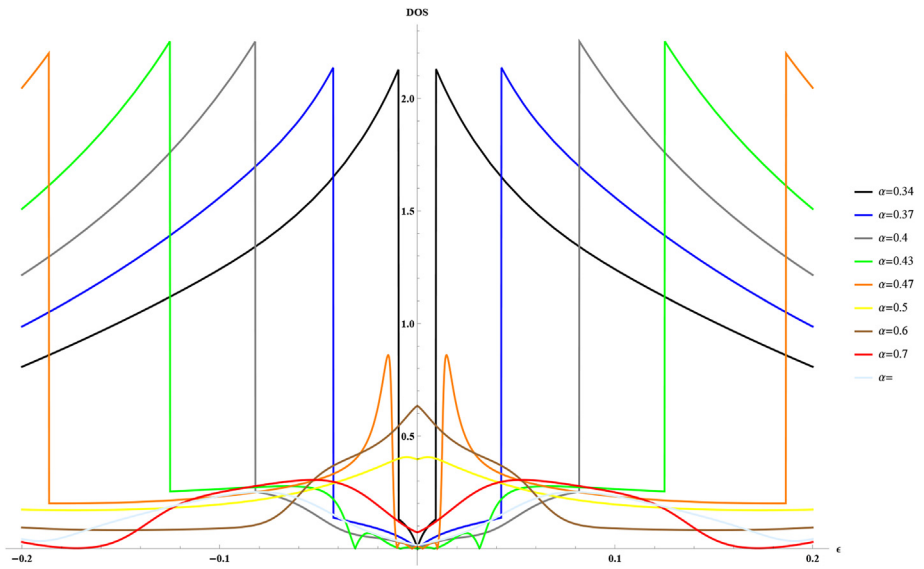

Fig. 7. Density of states for α between $\alpha = 0.34$ and $\alpha = 075$ for $k \to \infty$.

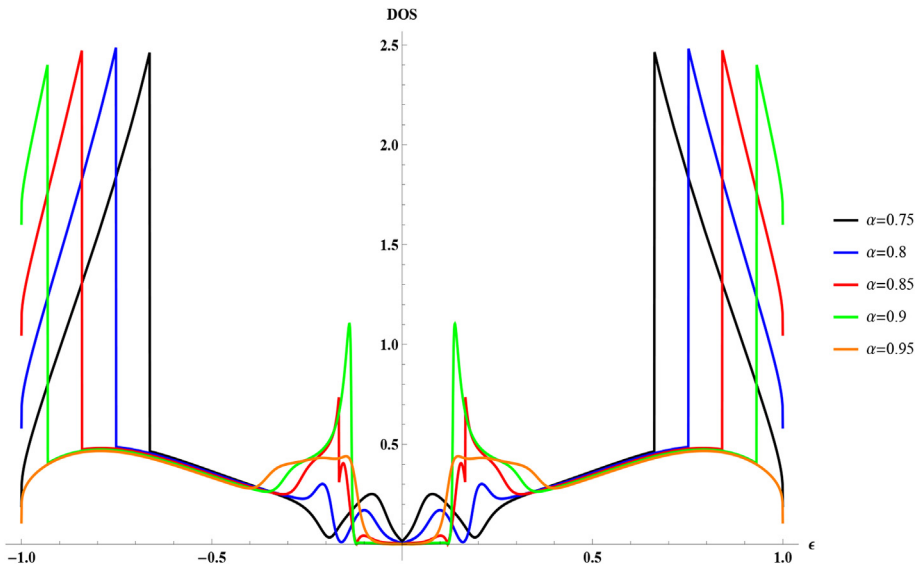

Fig. 8. Density of states for different values of α between 0.75 and 0.95 for $k \to \infty$. The signature of the Cantor distribution can be located around the Fermi level, where a set of resonances are shown.

on the impurity concentration as $\langle r \rangle \sim 1/c$. Then, for $\langle r \rangle \sim r_{imp}$ an overlap of the impurity states will be possible, which will activate the spectrum rearrangement. Using that $\langle v^2 \rangle_k = \frac{\alpha^2}{4} 3^{-2k-1}(2 \cdot 3^{2+k} + 16 \cdot 3^{2k+1} - 41)$, then critical concentration reads

$$c_{cr}^{(k)} = \frac{16}{\alpha^4 3^{-4k-2}\left(2 \cdot 3^{2+k} + 16 \cdot 3^{2k+1} - 41\right)^2} \tag{23}$$

for $k \to \infty$, the critical concentration of impurities reads

$$c_{cr}^{(\infty)} = \frac{16}{\alpha^4} \tag{24}$$

This critical concentration generates an impurity band which will manifest in the electronic density of states around the Fermi level. The key signature of the random Cantor distribution can be found in the impurity band formed below the Fermi

level, which shows small oscillations in the electronic density of states, which are given by the scale-periodic nature of the Cantor set.

4. Conclusions

The study of the defects in graphene-based materials is a very important field, especially for the purpose of fabricating devices, such as superlattices or multilayers. In turn, disorder plays a central role in all the observed electronic and magnetic properties of the material, then it is important to focus the way in which structured disorder can enhance or decrease the desired properties. In this work we have studied the electronic properties of Dirac electrons in graphene under a random Cantor distribution for the on-site energies of the impurities located at random positions. We have used the full T-matrix approximation to obtain the electronic density of states for different values of the iteration parameter k of the Cantor set. For values of $k \geq 2$, the DOS present a transition from a metallic phase to an insulator phase when the width α is increased. This metal-insulator transition appears as a Mott transition where a band splitting occurs after a divergence of the DOS at the Fermi level. In turn, it was shown that in the $k \to \infty$ limit, this behavior is enhanced, but in the insulator phase, the signature of the full-iterated Cantor distribution appears below and above the Fermi level as a sequence of resonances that splits in two more resonances when α reaches the limiting value $\alpha = 1$. In turn, we have found the critical concentration of impurities at which the random impurities overlap and forms the impurity band. This critical concentration depends on the width α as α^{-4} and has a minimum value of $16/\alpha^4$ for $k \to \infty$. These results are important to obtain the most important signatures of fractal-based structures in solid state physics.

Acknowledgment

This paper was partially supported by grants of CONICET (Argentina National Research Council) and Universidad Nacional del Sur (UNS) and by ANPCyT through PICT 1770, and PIP-CONICET Nos. 114-200901-00272 and 114-200901-00068 research grants, as well as by SGCyT-UNS., E.A.G., P.V.J. and J.S.A are members of CONICET. P.B.is a fellow researcher at this institution.

Appendix

In this Appendix, the first coefficient $\chi_2^{(k)}$ is computed. Using Eq. (15)

$$\chi_2^{(k)} = \sum_{i_1=0}^{1} \cdots \sum_{i_{k-1}=0}^{1} \sum_{l=0}^{1} \left[\left(\frac{2l(1-\delta_{k,0}) + 1 + 2\beta_k (1-\delta_{k,0})(1-\delta_{k,1})}{3^k} - \frac{1}{2} \right)^3 - \left(\frac{2l(1-\delta_{k,0}) + 2\beta_k (1-\delta_{k,0})(1-\delta_{k,1})}{3^k} - \frac{1}{2} \right)^3 \right] \tag{25}$$

The term inside the square bracket can be expanded in powers β_k as follows

$$\begin{aligned} &\sum_{l=0}^{1} \left[\left(\frac{2l(1-\delta_{k,0}) + 1 + 2\beta_k (1-\delta_{k,0})(1-\delta_{k,1})}{3^k} - \frac{1}{2} \right)^3 - \left(\frac{2l(1-\delta_{k,0}) + 2\beta_k (1-\delta_{k,0})(1-\delta_{k,1})}{3^k} - \frac{1}{2} \right)^3 \right] = \\ &= \frac{1}{2} \quad \text{for } k = 0 \\ &= \frac{13}{54} \quad \text{for } k = 1 \\ &= \frac{1}{2} 27^{-k} \left[40 + 3^{2k+1} - 2 \cdot 3^{k+2} \right] - 4 \cdot 3^{1-3k} \left(3^k - 3 \right) \beta_k + 8 \cdot 3^{1-3k} \beta_k^2 \quad \text{for } k > 1 \end{aligned} \tag{26}$$

$$\chi_2^{(k)} = \sum_{i_1=0}^{1} \cdots \sum_{i_{k-1}=0}^{1} \sum_{l=0}^{1} \left[-2 \cdot 3^{-2k} \left(3^k - 3 + 2\delta_{k,0} \right) + 8 \cdot 3^{-2k} \beta_k \right] \tag{27}$$

By noting that $\sum_{i_1=0}^{1} \cdots \sum_{i_{k-1}=0}^{1} 1 = 2^{k-1}$ and

$$\sum_{i_1=0}^{1} \cdots \sum_{i_{k-1}=0}^{1} \beta_k = 3 \cdot 2^{k-2} \left(3^k - 1 \right) \tag{28}$$

and

$$\sum_{i_1=0}^{1}\cdots\sum_{i_{k-1}=0}^{1}\beta_k^2 = 9\cdot 2^{k-5}\left(1-4\cdot 3^k+3^{1+2k}\right) \tag{29}$$

then

$$\chi_2^{(0)}=\frac{1}{4},\quad \chi_2^{(1)}=\frac{13}{54},\quad \chi_2^{(k>1)}=2^{k-2}3^{-3k}\left[2\cdot 3^{k+2}+16\cdot 3^{1+2k}-41\right] \tag{30}$$

For the different values of $\chi_n^{(k)}$, the main procedure is the same, the only complex algebraic manipulation is to compute $\sum_{i_1=0}^{1}\cdots\sum_{i_{k-1}=0}^{1}\beta_k^n$, which can be done with different computational software programs. In Section II we have computed up to $\chi_{12}^{(k)}$ to obtain reliable results.

References

[1] K.S. Novoselov, A.K. Geim, S.V. Morozov, D. Jiang, M.I. Katsnelson, I.V. Grigorieva, S.V. Dubonos, A.A. Firsov, Nature 438 (2005) 197.
[2] A.K. Geim, K.S. Novoselov, Nat. Mater. 6 (2007) 183.
[3] Y.B. Zhang, Y.W. Tan, H.L. Stormer, P. Kim, Nature 438 (2005) 201.
[4] A.H. Castro Neto, F. Guinea, N.M.R. Peres, K.S. Novoselov, A.K. Geim, Rev. Mod. Phys. 81 (2009) 109.
[5] M.O. Goerbig, Rev. Mod. Phys. 83 (2011) 4.
[6] J. McClure, Phys. Rev. 104 (1956) 666.
[7] V.P. Gusynin, S.G. Sharapov, Phys. Rev. Lett. 95 (2005) 146801.
[8] A.H. Castro Neto, F. Guinea, N.M.R. Peres, Phys. Rev. B 73 (2006) 205408.
[9] Y.-W. Tan, Y. Zhang, K. Bolotin, Y. Zhao, S. Adam, E.H. Hwang, S. Das Sarma, H.L. Stormer, P. Kim, Phys. Rev. Lett. 99 (2007) 246803.
[10] J.S. Ardenghi, P. Bechthold, P. Jasen, E. Gonzalez, A. Juan, Phys. B 452 (2014) 92–101.
[11] J.H. Chen, W.G. Cullen, C. Jang, et al., Phys. Rev. Lett. 102 (2009) 236805.
[12] A. Bostwick, J.L. McChesney, K.V. Emtsev, et al., Phys. Rev. Lett. 103 (2009) 056404.
[13] F. Withers, M. Dubois, A.K. Savchenko, Phys. Rev. B 82 (2010) 073403.
[14] F. Schedin, A.K. Geim, S.V. Moeozov, E.W. Hill, P. Blake, M.I. Katsnelson, K.S. Novoselov, Nat. Mater. 6 (2007) 652.
[15] I.I. Barbolina, K.S. Novoselov, S.V. Morozov, S.V. Dubonos, M. Missous, A.O. Volkov, D.A. Christian, I.V. Grigorieva, A.K. Geim, Appl. Phys. Lett. 88 (2006) 013901.
[16] A. Feher, S. Feodosyev, I. Gospodarev, O. Kotlyar, K. Kravchenko, E. Manzhelii, E. Syrkin, Superlatt. Microstruct. 53 (2013) 55–62.
[17] B.B. Mandelbrot, The Fractal Geometry of Nature, Freeman, San Francisco, CA, 1982.
[18] M.V. Feigel'man, L.B. Ioffe, V.E. Kravtsov, E.A. Yuzbashyan, Phys. Rev. Lett. 98 (2007) 027001.
[19] M.V. Feigel'man, L.B. Ioffe, V.E. Kravtsov, E. Cuevas, Ann. Phys. 325 (7) (2010) 1390–1478.
[20] I.S. Burmistrov, I.V. Gornyi, A.D. Mirlin, Phys. Rev. Lett. 108 (2012) 017002.
[21] S. Kettemann, E.R. Mucciolo, I. Varga, Phys. Rev. Lett. 103 (2009) 126401.
[22] Y. Gefen, B. Mandelbrot, A. Aharony, Phys. Rev. Lett. 45 (1980) 855.
[23] V.E. Kravtsov, O.M. Yevtushenko, P. Snajberk, E. Cuevas, Phys. Rev. E 86 (2012) 021136.
[24] C.T. Hill, Phys. Rev. D. 67 (2003) 085004.
[25] X. Sun, D.L. Jaggard, J. Appl. Phys. 70 (1991) 2500.
[26] M. Bertolotti, P. Masciulli, C. Sibilia, Opt. Lett. 19 (1994) 777.
[27] M. Bertolotti, P. Masciulli, C. Sibilia, F. Wijnands, H. Hoekstra, J. Opt. Soc. Am. B 13 (1996) 628.
[28] F. Chiadini, V. Fiumara, I.M. Pinto, A. Scaglione, Microw. Opt. Technol. Lett. 37 (2003) 339.
[29] F.R. Lad, W.F.C. Taylor, Statistics Probab. Lett. 13 (1992) 307–310.
[30] K.A. Makarov, J. Math. Phys. 35 (1994) 1522.
[31] N.L. Chuprikov, J. Phys. A Math. Gen. 33 (2000) 4293.
[32] N.L. Chuprikov, D.N. Zhabin, J. Phys. A Math. Gen. 33 (2000) 4309.
[33] J.A. Monsoriu, F.R. Villatoro, M.J. Marín, J.F. Urchueguía, P. Fernández de Córdoba, Eur. J. Phys. 26 (2005) 603.
[34] K. Esaki, M. Sato, M. Kohmoto, Phys. Rev. E 79 (2009) 056226.
[35] Z. Xiao, Z. Wang (English Edition), J. Shanghai Univ. 15 (1) (2011) 35–37.
[36] L. Sun, C. Fang, Y. Song, Y. Guo, J. Phys. Condens. Matter 22 (2010) 445303.
[37] R. Rodríguez-González, J.C. Martínez-Orozco, J. Madrigal-Melchor, I. Rodríguez-Vargas, AIP Conf. Proc. 1598 (2014) 55.
[38] O. Dovgosheya, O. Martio, V. Ryazanova, M. Vuorinenc, Expo. Math. 24 (2006) 1–37.
[39] J. Korringa, J. Phys. Chem. Solids 7 (1958) 252.
[40] J. Beeby, Proc. Phys. Soc. Lond. A279 (1964) 82.
[41] J. Beeby, Phys. Rev. A130 (1964) 135.
[42] J.S. Ardenghi, P. Bechthold, E. Gonzalez, P. Jasen, A. Juan, Superlattices Microstruct. 72 (2014) 325–335.
[43] N.A. Pike, D. Stroud, Phys. Rev. B 89 (2014) 115428.
[44] N.M.R. Peres, F. Guinea, A.H. Castro Neto, Phys. Rev. B 73 (2006) 125411.
[45] F. Chovanec, Sci. Mil. 5 (1) (2010) 5–10.
[46] R.J. Elliott, J.A. Krumhansl, P.L. Leath, Rev. Mod. Phys. 46 (1974) 465.
[47] N.H. Shon, T. Ando, J. Phys. Soc. Jpn. 67 (1998) 2421.
[48] H. Kumazaki, D.S. Hirashima, J. Phys. Soc. Jpn. 75 (2006) 5.
[49] T.O. Wehling, A.V. Balatsky, M.I. Katsnelson, A.I. Lichtenstein, K. Scharnberg, R. Wiesendanger, Phys. Rev. B 75 (2007) 125425.
[50] B.Y. Hu, E.H. Hwang, S. Das Sarma, Phys. Rev. B 78 (2008) 165411.
[51] E.N. Economou, Green's Functions in Quantum Physics, second ed., Springer, Berlin (, 1979.
[52] L. Capriotti, D.J. Scalapino, R.D. Sedgewick, Phys. Rev. B 68 (2003) 014508.
[53] E.H. Hwang, S. Adam, S. Das Sarma, Phys. Rev. Lett. 98 (2007) 186806.
[54] S. Adam, E.H. Hwang, V.M. Galitski, S. Das Sarma, Proc. Natl. Acad. Sci. U.S.A. 104 (2007) 18392.
[55] S.S. Pershoguba, Y.V. Skrypnyk, V.M. Loktev, Phys. Rev. B 80 (2009) 214201.
[56] Y. Skrypnyk, J. Non-Crystalline Sol. 352 (2006) 4325–4330.